Design of a Novel Self-Balancing Mechanism on AGV for Stable Stair Climbing .

Yue Feng[1], Huiming Wang[1,2], Jing Wu[1], Hanyu Song[1] and I-Ming Chen[1] *Fellow, IEEE*
1. School of Mechanical and Aerospace Engineering, Nanyang Technological University, 639798, Singapore
Email: yue.feng@ntu.edu.sg; MICHEN@ntu.edu.sg
2. School of Automation, Chongqing University of Posts and Telecommunications, Chongqing, 400065, China
Email: wanghm@cqupt.edu.cn

***Abstract*—Task space beyond 2D planes brings challenges to the traditional automated guided vehicle (AGV) on goods delivery. In this paper, a novel self-balancing platform is designed for the stable stair climbing of AGV. While the AGV is moving in a constructional site, this mechanism enhances the AGV to handle heavy payload or even carry another operating robot, through keeping them horizontal to the ground over time. In the design, the two degree-of-freedom (DOF) of this mechanism allows the platform to rotate around two mutually perpendicular axes. The rotation ranges are $[-15^\circ, 15^\circ]$ and $[0^\circ, 40^\circ]$, respectively. Through the feedback of an inertial measurement unit (IMU), the self-balancing control can be achieved. The demonstration show that the workspace not only allows the mechanism to reduce the vibration acting on the carried goods when the AGV is driving on uneven terrain but also allows the platform to maintain the center of gravity (CG) while the AGV is climbing.**

***Index Terms*—construction robotics, intelligent robotic system, self-balancing platform, parallel mechanism.**

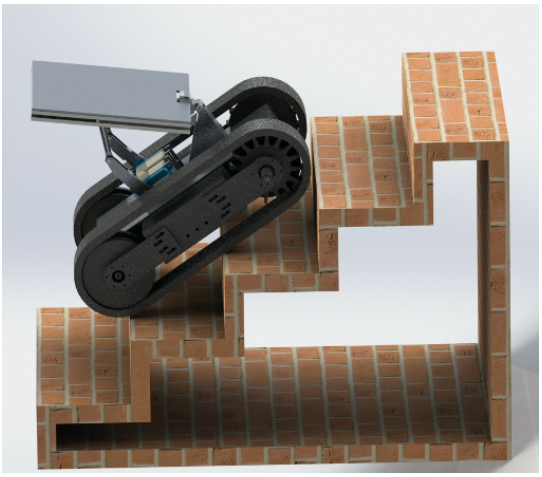

Fig. 1. Illustration of this work.

I. Introduction

The progress of robotic technologies has facilitated automation in many industries, such as manufacturing [1], logistics [2], exploration [3], etc. In recent years, with the development of perception [4] and intelligent control [5], robotic systems have been gradually deployed in the construction area [6].

In traditional, the goods delivery for automated guided vehicle (AGV) only needs to face navigation issues in 2D environments. In the construction site, however, 3D environments such as stairs and uneven terrain bring unavoidable challenges. Stable stair climbing has become a hot topic in robotics, various types of mechanical structures have been designed to enable robots to be adaptive to such scenarios, such as leg-based [7], wheel-leg-based [8] [9] and track-based [10] type. While the robots can move on the stairs, the adopted strategies to dynamically keep the goods steady on the robots during the motion are also vital. Firstly, when the robot is carrying the heavy goods (as well as goods with large size) on stair climbing, the deviation of center of gravity (CG) may make the overall entity flip over. Secondly, when the carried goods are an operating robot, the performance of stable motion performed by the AGV impacts the operation of the carried robot.

This work was supported in part by National Robotics Program, RDS, SERC, Singapore (1922200001).

Inspired by this issue, the design of a detachable self-balancing platform for the aforementioned purpose is needed. A popular mechanical structure for the design of self-balancing platforms is parallel kinematic mechanism (PKM) because of its loading capacity, dynamic reaction, and compactness. The theory of PKM has been explored in many studies for decades and has various derivative forms that have been widely used in many applications, such as vehicle driving simulators [11] [12], industrial high-speed pick-and-place machines [13], micro-motion manipulators [14]. In spite of the vast amount of literature on self-balancing platform, there is no existing self-balancing platform design that can be directly implemented in the aforementioned scenario. Thus, this paper proposes a novel two degree-of-freedom (DOF) PKM that can facilitate goods delivery in stair climbing, as shown in Fig. 1, whose main functions is transporting goods or another wall grinding robot in stairs scenarios. The designed mechanism can keep the CG of the overall robotic system through adjustment based on an attached inertial measurement unit (IMU). Besides, the self-balancing platform has a wide range workspace spanned by two DOF to cope with more types of stairs.

The remainder of this paper is organized as follows: Section II describes the kinematic design of the self-balancing platform. Section III provides the kinematics and force analy-

978-1-7281-5414-5/20/$31.00 ©2020 IEEE

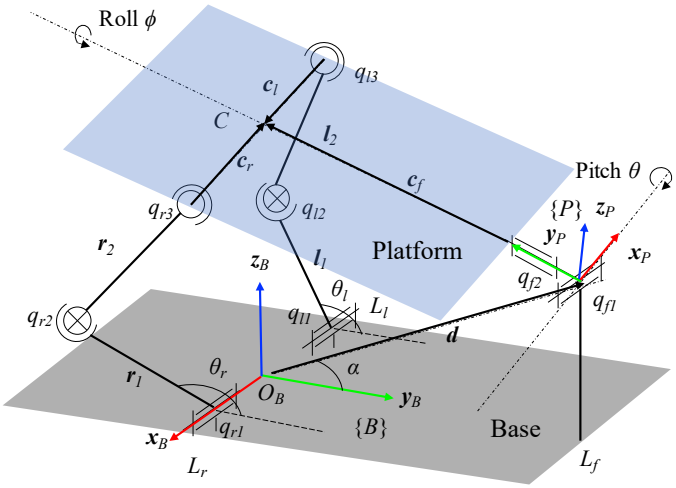

Fig. 2. Topological kinematics of self-balancing platform.

sis on the design and explain how the key dimensions and maximum payload of the structure can be computed. Section IV shows the prototype, simulation results on kinematics, and the demonstration, to validate the feasibility of the mechanism. Section V briefly concludes this work.

II. Conceptual Design

A. Overall structure

The PKM proposed in this paper is given in Fig. 2, which is composed of five parts: the base, the platform, the front linkage L_f, the right linkage L_r, and left linkage L_l. All of the three linkages connects the base and the platform. L_f consists of two rotational joints q_{f1} and q_{f2} that are perpendicular to each other. Each of L_r and L_l contains a rotational joint (q_{r1} and q_{l1}), a universal joint (q_{r2} and q_{l2}), and one spherical joint (q_{r3} and q_{l3}) that are also in serial.

The rotation axes of joints q_{r1} and q_{l1} are co-linear, which is also parallel to the rotation axis of joint q_{f1}. The origin of the base frame $\{B\}$ is selected as the middle point between q_{r1} and q_{l1}. The $\boldsymbol{x}_B$ coincides with the rotation axes of both q_{r1} and q_{l1}, while the axis $\boldsymbol{z}_B$ is perpendicular to the base. The platform frame is defined as $\{P\}$, where its origin is selected at q_{f1} and is determined by a vector $\boldsymbol{d}$. Note that the projection of $\boldsymbol{d}$ on the plane $\boldsymbol{x}_B - \boldsymbol{y}_B$ is along $\boldsymbol{y}_B$, and the axis $\boldsymbol{y}_p$ coincides with rotation axis of joint q_{f2}. When $\boldsymbol{x}_P$ parallel to $\boldsymbol{x}_B$, the mechanism is symmetrical to the $y-z$ plane of $\{B\}$. For linkage L_r and L_l, both of $\boldsymbol{r}_1$ and $\boldsymbol{l}_1$ are perpendicular to the axis $\boldsymbol{x}_B$. Besides, the symmetry of L_r and L_l holds, which means $|\boldsymbol{r}_1| = |\boldsymbol{l}_1|$ and $|\boldsymbol{r}_2| = |\boldsymbol{l}_2|$. In addition, the spherical joints q_{r3} and q_{l3} are designed to connect the platform. Both $\boldsymbol{c}_r$ and $\boldsymbol{c}_l$ are perpendicular to the axis $\boldsymbol{y}_P$, and the intersection is the middle point between q_{r3} and q_{l3}, called C. The vector from q_{f1} to C is denoted as $\boldsymbol{c}_f$. Similarly, because of the symmetry, $|\boldsymbol{c}_r| = |\boldsymbol{c}_l|$.

The overall design has two rotational joints for motor driving. Considering to get the possible largest loading on the platform with limited torque supply, the two motors drive the joints q_{r1} and q_{l1}, where the corresponding driving angle are denoted as θ_r and θ_l.

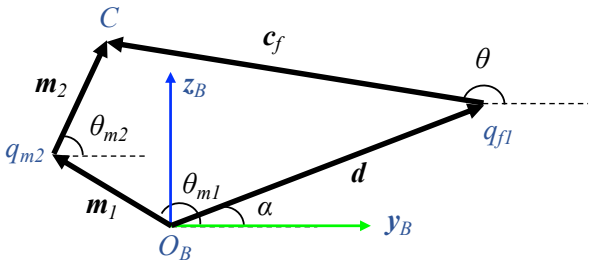

Fig. 3. Side-view of self-balancing platform.

B. Design of pitch angle

To simplify the workspace analysis in the direction of pitch, the input values of θ_r and θ_l are assumed to be identical all the time, which maintains the roll angle ϕ at π. Changing the view from 3D to 2D, as illustrated in the Fig. 3, the designed structure can be taken as a typical four-bar linkage which is the projection of L_r and L_l on the plane $\boldsymbol{y}_B - \boldsymbol{z}_B$. The angles between the vectors $\boldsymbol{d}$, $\boldsymbol{m}_1$, $\boldsymbol{m}_2$ and the axis $\boldsymbol{y}_B$ are denoted as α, θ_{m1}, θ_{m2}, respectively. Besides, the pitch angle θ is equal to the angle between $\boldsymbol{c}_f$ and $\boldsymbol{y}_B$.

The following relation can be derived from Fig. 3:

$$\boldsymbol{m}_1 + \boldsymbol{m}_2 = \boldsymbol{d} + \boldsymbol{c}_f,$$

where

$$\begin{cases} \boldsymbol{m}_1 = (0, |\boldsymbol{m}_1|\cos\theta_{m1}, |\boldsymbol{m}_1|\sin\theta_{m1}) \\ \boldsymbol{m}_2 = (0, |\boldsymbol{m}_2|\cos\theta_{m2}, |\boldsymbol{m}_2|\sin\theta_{m2}) \\ \boldsymbol{d} = (0, |\boldsymbol{d}|\cos\alpha, |\boldsymbol{d}|\sin\alpha) \\ \boldsymbol{c}_f = (0, |\boldsymbol{c}_f|\cos\theta, |\boldsymbol{c}_f|\sin\theta) \end{cases}.$$

Thus,

$$\begin{cases} |\boldsymbol{m}_1|\sin\theta_{m1} + |\boldsymbol{m}_2|\sin\theta_{m2} = |\boldsymbol{d}|\sin\alpha + |\boldsymbol{c}_f|\sin\theta \\ |\boldsymbol{m}_1|\cos\theta_{m1} + |\boldsymbol{m}_2|\cos\theta_{m2} = |\boldsymbol{d}|\cos\alpha + |\boldsymbol{c}_f|\cos\theta \end{cases}. \tag{1}$$

The pitch angle θ is one of the most critical variable in this mechanism, which limits the maximum slope of stairs that the AGV can climb. In order to determine the dimensions of the links, the range of inputs and outputs should be obtained in advance: $\theta_{m1} \in [\theta^U_{m1}, \theta^L_{m1}]$ and $\theta \in [\theta^U, \theta^L]$. Next on, the values of $|\boldsymbol{d}|$ and α are designed based on user requirements. Finally, the dimensions of $|\boldsymbol{m}_1|$, $|\boldsymbol{m}_2|$, and $|\boldsymbol{c}_f|$, can be calculated.

Fig. 4 shows the configurations of the pitch angle in two cases, where U refers to the upper case (the platform is active) and L refers to the lower case (the platform is inactive). In Fig. 4 (a), $\theta = \theta^U$ and the links $\boldsymbol{m}_1$ and $\boldsymbol{m}_2$ are co-linear, where $[\theta_{m1}, \theta_{m2}] = [\theta^U_{m1}, \theta^U_{m2}] = [\theta^U_{m1}, \theta^U_{m1}]$. In Fig. 4 (b), $\theta = \theta^L$, it has $[\theta_{m1}, \theta_{m2}] = [\theta^L_{m1}, \theta^L_{m2}]$.

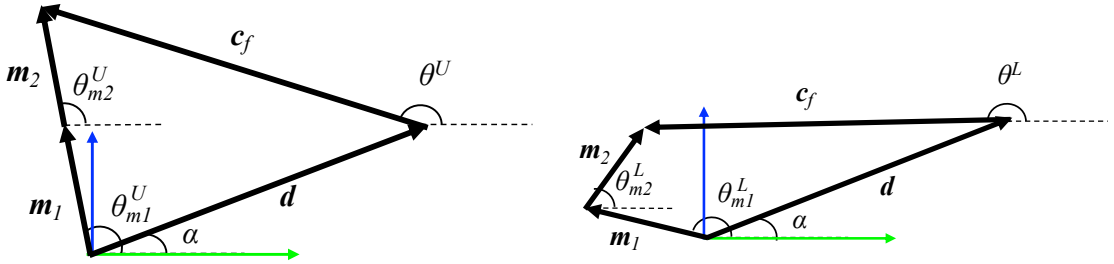

(a) Upper case (active) (b) Lower case (inactive)

Fig. 4. Output angle θ in upper and lower cases .

Since there are two cases, (1) governs four equations with four unknown parameters:

$$\begin{cases} |\boldsymbol{m}_1|\sin\theta^U_{m1} + |\boldsymbol{m}_2|\sin\theta^U_{m2} = |\boldsymbol{d}|\sin\alpha + |\boldsymbol{c}_f|\sin\theta^U \\ |\boldsymbol{m}_1|\cos\theta^U_{m1} + |\boldsymbol{m}_2|\cos\theta^U_{m2} = |\boldsymbol{d}|\cos\alpha + |\boldsymbol{c}_f|\cos\theta^U \\ |\boldsymbol{m}_1|\sin\theta^L_{m1} + |\boldsymbol{m}_2|\sin\theta^L_{m2} = |\boldsymbol{d}|\sin\alpha + |\boldsymbol{c}_f|\sin\theta^L \\ |\boldsymbol{m}_1|\cos\theta^L_{m1} + |\boldsymbol{m}_2|\cos\theta^L_{m2} = |\boldsymbol{d}|\cos\alpha + |\boldsymbol{c}_f|\cos\theta^L \end{cases},$$

where $|\boldsymbol{m}_1|$, $|\boldsymbol{m}_2|$, θ^L_{m2}, and $|\boldsymbol{c}_f|$, are the unknown variables need to solve, and the remaining are pre-determined. Normally, there is only one exact solution for this unknown set if the given configuration can be achieved.

Remark 1. Once the dimensions are determined, taking θ and θ^L_{m2} as unknowns, θ_{m1} as input variable, a function $\theta = u(\theta_{m1})$ can be designed to control the pitch angle of the platform. However, there are more than one solution sets for the unknowns. By using computer to solve these equations, the initial guess is required, which can be selected as $[\theta_{m1}, \theta] = [(\theta^L_{m1} + \theta^U_{m1})/2, (\theta^L + \theta^U)/2]$.

C. Design of roll angle

Different from the pitch angle, roll angle of the platform provides additional DOF. The design objective of this DOF is to allow the platform to remain horizontal to the ground in another direction, when the AGV is misaligned to the expected moving direction on the stairs or encounters uneven terrain. Besides, it can also help the AGV reduce the vibration. Thus, the required range of roll can be narrower than pitch.

After determining $\{|\boldsymbol{m}_1|, |\boldsymbol{m}_2|, |\boldsymbol{c}_f|, |\boldsymbol{d}|, \alpha, \theta^L_{m1}, \theta^U_{m1}, \theta^U, \theta^L\}$ from the design of pitch angle, there is only one parameter that can affect the roll angle ϕ: $|\boldsymbol{c}_r|$, which also equals to $|\boldsymbol{c}_l|$. It can be obtained by

$$\begin{aligned} r_{2x}^2 + r_{2y}^2 + r_{2z}^2 &= |\boldsymbol{r}_2|^2 = |\boldsymbol{m}_2|^2 \\ l_{2x}^2 + l_{2y}^2 + l_{2z}^2 &= |\boldsymbol{l}_2|^2 = |\boldsymbol{m}_2|^2, \end{aligned} \tag{2}$$

where

$$\boldsymbol{r}_2 = \begin{bmatrix} -|\boldsymbol{c}_r|\cos\phi - |\boldsymbol{c}_r| \\ |\boldsymbol{d}|\ \cos\alpha + |\boldsymbol{c}_f|\cos\theta - |\boldsymbol{r}_1|\cos\theta_r \\ |\boldsymbol{d}|\sin\alpha + |\boldsymbol{c}_f|\sin\theta - |\boldsymbol{c}_r|\sin\phi - |\boldsymbol{r}_1|\sin\theta_r \end{bmatrix}$$

and

$$\boldsymbol{l}_2 = \begin{bmatrix} |\boldsymbol{c}_l|\cos\phi + |\boldsymbol{c}_l| \\ |\boldsymbol{d}|\cos\alpha + |\boldsymbol{c}_f|\cos\theta - |\boldsymbol{l}_1|\cos\theta_l \\ |\boldsymbol{d}|\sin\alpha + |\boldsymbol{c}_f|\sin\theta + |\boldsymbol{c}_l|\sin\phi - |\boldsymbol{l}_1|\sin\theta_l \end{bmatrix}.$$

Assume that θ_r and θ_l are identical to the two designed angles in their domains, says $[\theta_r, \theta_l] = [\theta_a, \theta_b]$ has a corresponding output $\phi = \phi_1$ and $[\theta_r, \theta_l] = [\theta_b, \theta_a]$ has a corresponding output $\phi = \phi_2$. Due to the nature of symmetry, $|\phi_1 - \pi| = |\phi_2 - \pi| = \Delta\phi$.

In order to calculate the dimensions of $|\boldsymbol{c}_r|$ and $|\boldsymbol{c}_l|$, $\Delta\phi$ has to be determined in advance. The same dimensions can be obtained no matter choosing $\phi = \phi_1$ or $\phi = \phi_2$ and their corresponding input angles.

Remark 2. Taking $\phi = \phi_1$ as an example, there exist known parameters, $\{|\boldsymbol{r}_1|, |\boldsymbol{r}_2|, |\boldsymbol{l}_1|, |\boldsymbol{l}_2|, |\boldsymbol{c}_f|, |\boldsymbol{d}|, \alpha\}$, designed values $\{\theta_a, \theta_b\}$ and two unknowns (intermediate value θ and desired value $|\boldsymbol{c}_r|$ which equals to $|\boldsymbol{c}_l|$). Substituting these values into (2), it yields two equations that contains two unknowns. Normally, it has multiple sets of solutions. To compute this equation set, initial guesses can be $[\theta, |\boldsymbol{c}_r|] = [(\theta^L + \theta^U)/2, |\boldsymbol{d}|]$. Note that if there is no solution, then the configuration does not exist.

Remark 3. By using (2), the solutions of forward and inverse kinematics can also be obtained. For forward kinematics, the input values are $\{\theta_r, \theta_l\}$, while the output values are $\{\theta, \phi\}$. The seven known parameters mentioned in the last paragraph remains unchanged. Substituting unknowns and known values into (2), functions $\theta = \mathcal{F}_\theta(\theta_r, \theta_l)$ and $\Delta\phi = \mathcal{F}_{\Delta\phi}(\theta_r, \theta_l)$ can be designed and the initial guess can be selected as $[\theta, \Delta\phi] = [(\theta^L + \theta^U)/2, 0]$. For inverse kinematics, functions $\theta_r = \mathcal{I}_{\theta_r}(\theta, \phi)$ and $\theta_l = \mathcal{I}_{\theta_l}(\theta, \phi)$ can be designed by the similar method and the initial guess can be selected as $[\theta_r, \theta_l] = [(\theta^L_{m1} + \theta^U_{m1})/2, (\theta^L_{m1} + \theta^U_{m1})/2]$. Note that the solutions are not unique.

III. Force Analysis

When the required load is acting on the platform, the stress limits of all joints and links are far larger than the actual stresses. Due to the size and power limitation of the mechanism, however, the input torques from motor q_{r1} and q_{l1} are the bottlenecks. Therefore, this section presents a method to find the maximum input torques τ^R_{max} and τ^L_{max}, by treating θ_r, θ_l, vectors of multiple loading forces, and their lever arms as input elements.

A. Single force analysis

One more coordinate is established at q_{f1}, denoted as $\{P'\}$, where the axis $\boldsymbol{x}_{P'}$ coincides with the rotation axis of q_{f1}, and

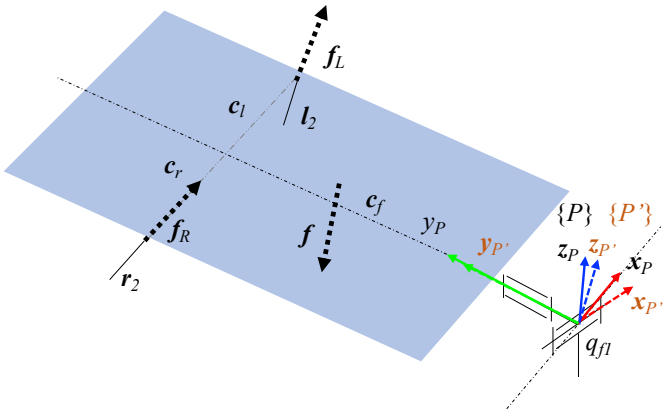

Fig. 5. Illustration of single loading force.

$\boldsymbol{y}_{P'}$ coincides with $\boldsymbol{y}_P$, as shown in Fig. 5.

First of all, two homogeneous transformation matrices, $\boldsymbol{R}^B_{P'}$ (from $\{B\}$ to $\{P'\}$) and $\boldsymbol{R}^P_{P'}$(from $\{P\}$ to $\{P'\}$), are defined as follows:

$$\boldsymbol{R}^B_{P'} = \begin{bmatrix} -1 & 0 & 0 \\ 0 & \cos\theta & -\sin\theta \\ 0 & -\sin\theta & -\cos\theta \end{bmatrix} \in SO(3)$$
$$\boldsymbol{R}^P_{P'} = \begin{bmatrix} -\cos\phi & 0 & \sin\phi \\ 0 & 1 & 0 \\ -\sin\phi & 0 & -\cos\phi \end{bmatrix} \in SO(3)$$

In Fig. 5, there are four vectors in frame $\{P\}$: $\{\boldsymbol{r}_R, \boldsymbol{r}_L, \boldsymbol{f}, \text{ and } \boldsymbol{r}_f\}$. $\boldsymbol{r}_R$ and $\boldsymbol{r}_L$ are the lever arms of forces $\boldsymbol{f}_R$ and $\boldsymbol{f}_L$. $\boldsymbol{r}_f$ is the lever arm of the loading force $\boldsymbol{f}$ that is always perpendicular to the plane $\boldsymbol{x}_P - \boldsymbol{y}_P$. During operating, the platform is expected to be always perpendicular to the direction of gravity. By transforming these four vectors from $\{P\}$ to $\{P'\}$, they are represented by

$$\boldsymbol{r}^*_R = \boldsymbol{R}^P_{P'}[-|\boldsymbol{c}_r|, |\boldsymbol{c}_f|, 0]^T \quad \boldsymbol{r}^*_L = \boldsymbol{R}^P_{P'}[|\boldsymbol{c}_l|, |\boldsymbol{c}_f|, 0]^T$$
$$\boldsymbol{f}^* = \boldsymbol{R}^P_{P'}[0, 0, -|\boldsymbol{f}|]^T \quad \boldsymbol{r}^*_f = \boldsymbol{R}^P_{P'}[r_{fx}, r_{fy}, 0]^T$$

In frame $\{B\}$, vectors $\boldsymbol{f}_R$ and $\boldsymbol{f}_L$ are the supporting forces from links $\boldsymbol{r}_2$ and $\boldsymbol{l}_2$. $\boldsymbol{n}_R$ and $\boldsymbol{n}_L$ are the unit vectors of $\boldsymbol{r}_2$ and $\boldsymbol{l}_2$ that can be calculated from (2). By transforming these vectors from the $\{B\}$ to $\{P'\}$, they are represented by

$$\boldsymbol{f}^*_R = |\boldsymbol{f}_R| \cdot \boldsymbol{R}^B_{P'} \cdot \boldsymbol{n}_R$$
$$\boldsymbol{f}^*_L = |\boldsymbol{f}_L| \cdot \boldsymbol{R}^B_{P'} \cdot \boldsymbol{n}_L$$

In frame $\{P'\}$, moment $\boldsymbol{M}_{P'}$ exerting at point q_{f1} has components on $\boldsymbol{x}_{P'}$ and $\boldsymbol{y}_{P'}$, which both equal to zero due to the rotation of joint q_{f1} and q_{f2}. Thus, it has

$$\boldsymbol{M}_{P'} = \boldsymbol{r}^*_f \times \boldsymbol{f}^* + \boldsymbol{r}^*_R \times \boldsymbol{f}^*_R + \boldsymbol{r}^*_L \times \boldsymbol{f}^*_L = \begin{bmatrix} 0 \\ 0 \\ . \end{bmatrix}. \quad (3)$$

(3) governs two equations, which contains two unknowns: $|\boldsymbol{f}_R|$ and $|\boldsymbol{f}_L|$. By finding the roots of the equation set, there is one certain solution set for the unknowns.

In frame $\{B\}$, forces acting on points q_{r2} and q_{l2} equal to $-\boldsymbol{f}_R$ and $-\boldsymbol{f}_L$, respectively. Thus, the moments generated by the right motor and left motor are

$$\begin{aligned} \boldsymbol{\tau}_R &= \boldsymbol{r}_1 \times |\boldsymbol{f}_R| \cdot \boldsymbol{n}_R \\ \boldsymbol{\tau}_L &= \boldsymbol{l}_1 \times |\boldsymbol{f}_L| \cdot \boldsymbol{n}_L \end{aligned}. \quad (4)$$

In summary, following the above flow, substituting all parameters in these equations, the functions $\boldsymbol{\tau}_R = \mathcal{M}_R(\theta_r, \theta_l, |\boldsymbol{f}|, \boldsymbol{r}_f)$, $\boldsymbol{\tau}_L = \mathcal{M}_L(\theta_r, \theta_l, |\boldsymbol{f}|, \boldsymbol{r}_f)$ can be designed. Because the required torques that supplied by the motors only along the direction of $\boldsymbol{x}_B$, the designed two functions only output the first element of $\boldsymbol{\tau}_R$ and $\boldsymbol{\tau}_L$, i.e. τ_{Rx} and τ_{Lx}.

B. Multiple force analysis

When the goods randomly placed on the platform, it forms n different forces at different locations on the plane. Each of these forces contributes moments to the points of motors:

$$\begin{aligned} \mathcal{T}_R(\theta_r, \theta_l) &= \sum_{i=1}^{n} \tau_{Rx}(\theta_r, \theta_l, |\boldsymbol{f}_i|, \boldsymbol{r}_{fi}) \\ \mathcal{T}_L(\theta_r, \theta_l) &= \sum_{i=1}^{n} \tau_{Lx}(\theta_r, \theta_l, |\boldsymbol{f}_i|, \boldsymbol{r}_{fi}) \end{aligned}. \quad (5)$$

Both the domains of θ_r and θ_l are $[\theta^U_{m1}, \theta^L_{m1}]$. Within these domains, finding the maximum torque τ^R_{max}, τ^L_{max} acting on the two motors in all possible positions of the platform is equivalent to finding the maximum values of $\mathcal{T}_R$ and $\mathcal{T}_L$, where

$$\begin{aligned} \tau^R_{max} &= \max \mathcal{T}_R(\theta_r, \theta_l) \\ \tau^L_{max} &= \max \mathcal{T}_L(\theta_r, \theta_l) \end{aligned}, \qquad \theta_r, \theta_l \in [\theta^U_{m1}, \theta^L_{m1}]. \quad (6)$$

IV. Experiments

The designed self-balancing platform is equipped on an AGV to realize self-balancing while the robot is transporting goods. Based on the kinematics and static analysis proposed in this paper, a prototype is designed and developed.

A. Prototype

For the convenience in fabrication, the universal joints (q_{r2} and q_{l2}) are placed by two spherical joints. It gives two more DOF to the mechanism that are self rotating around $\boldsymbol{r}_2$ and $\boldsymbol{l}_2$. This minor modification does not affect other performances.

Based on the proposed design of pitch angle, to calculate the dimensions of links $\{|\boldsymbol{m}_1|, |\boldsymbol{m}_2|, |\boldsymbol{c}_f|\}$, the parameters $\{\theta^U, \theta^L, |\boldsymbol{d}|, \alpha, \theta^U_{m1}, \theta^L_{m1}\}$ have to be determined first.

The inclination of tested stairs is $25°$. Thus, the range of pitch angle $[\theta^U, \theta^L]$ is designed as $[140°, 180°]$, allowing the AGV to move on the stairs that has inclination from $0°$ to $40°$. It also gives the surplus pitch angle to resist the vibration, while the AGV is on the stairs.

Parameters $\{|\boldsymbol{d}|, \alpha, \theta^U_{m1}, \theta^L_{m1}\}$ are determined by the specifications of the selected motor (Tonegawa-Seiko high-torque servo motor SSPS-105), which has $[-45°, 45°]$ operating range. Based on this, parameters $[|\boldsymbol{d}|, \alpha, \theta^U_{m1}, \theta^L_{m1}] = [200 \text{ mm}, 20°, 190°, 100°]$ can be obtained. By substituting

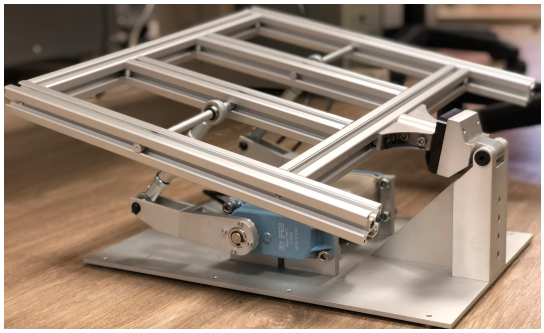

Fig. 6. Prototype of self-balancing platform.

these parameters into (1), which yields $[|\boldsymbol{m}_1|, |\boldsymbol{m}_2|, |\boldsymbol{c}_f|] \simeq [164 \text{ mm}, 106 \text{ mm}, 306 \text{ mm}]$.

For the design of roll angle, the objective is to find a suitable dimension for $|\boldsymbol{c}_r|$ or $|\boldsymbol{c}_l|$. When the robot is on the stairs that have $25°$ slope, the platform has position $\phi = 180°$ and $\theta = 165°$. Computed by (1), the input angles should be around $160°$. Hence, let $[\theta_a, \theta_b, \Delta\phi] = [170°, 150°, 15°]$, indicating that when $\phi = 180°$ and $\theta = 165°$, the two input motors rotate in opposite direction for $10°$ each, it will result in $\pm 15°$ change of ϕ. Thus, when the robot is on the stairs, the platform will have relatively fast responses regarding to sudden vibration from roll direction. Substituting these values into (2), $|\boldsymbol{c}_r| = |\boldsymbol{c}_l| \simeq 121$ mm can be obtained.

This prototype is equipped with an IMU (MPU-6050) and a microprocessor (Arduino Mega 2560). The IMU is installed on the upper moving platform (align to the platform coordinate) to capture the orientation of the platform. Through the comparison with the inertial reference frame, the orientation of the platform captured from this IMU are recorded for the feedback control, where the control loop is running at 50 Hz.

In summary, based on the proposed methods in this paper and the actual design requirements, the critical dimensions of this prototype are determined. According to the results, prototype is fabricated, as shown in Fig. 6.

B. Forward kinematics simulation

Fig. 7 illustrate the forward kinematic simulation results of $\theta = \mathcal{F}_\theta(\theta_r, \theta_l)$ and $\Delta\phi = \mathcal{F}_{\Delta\phi}(\theta_r, \theta_l)$, based on the dimensions of this prototype design. All the points at the graphs are the computational results by solving (2), where $\{\theta_r, \theta_l\}$ are taken as inputs and the resolutions are both $1°$. The plots demonstrate that the solutions are continuous and meet the requirements. Due to the geometry of the mechanism, the two surfaces are both symmetrical about the line $\theta_r = \theta_l$, which also validate the consistency. In Fig. 8 (a), the pitch angle is from $140°$ to $180°$ when $\theta_r = \theta_l = 100°$ and $\theta_r = \theta_l = 190°$. As the θ_r and θ_l increase, the output θ also increases. However, the increasing rate are different at different points. In Fig. 8 (b), the absolute roll angle is within $[0°, 50°]$. When $\theta_r = \theta_l$, the output $\Delta\phi$ always equal to zero. The maximum point is $\Delta\phi = \mathcal{F}_{\Delta\phi}(115°, 190°)$ instead of $\Delta\phi = \mathcal{F}_{\Delta\phi}(100°, 190°)$. If a point is at the convex and

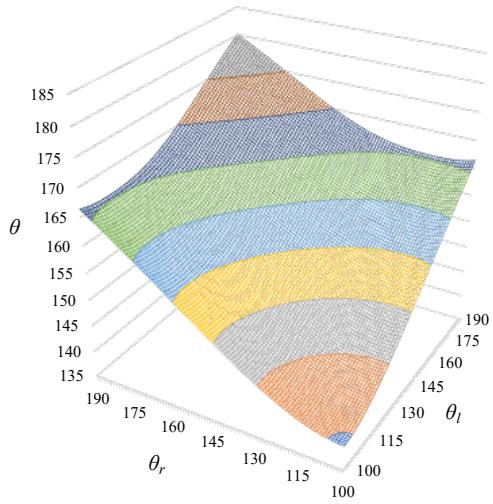

(a)

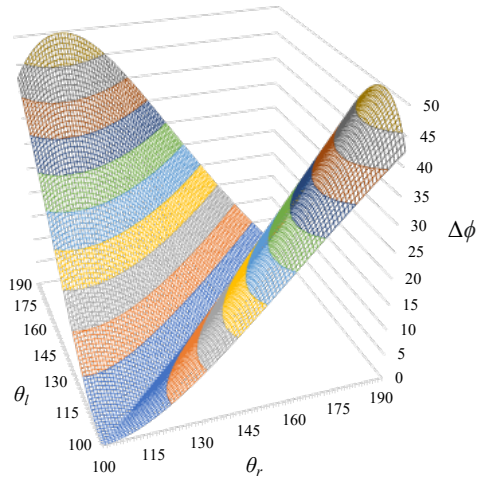

(b)

Fig. 7. Forward kinematics of self-balancing platform (units: degree).

moves toward the opposite direction from the middle concave, the roll angle will change from increasing to decreasing because the higher linkage has angle between link $\boldsymbol{r}_2$ (or $\boldsymbol{l}_2$) and axis $\boldsymbol{y}_B$ larger than inputs angle θ_r (or θ_l). It happens only when $|\theta_r - \theta_l| > 70°$. However, the range of spherical joints $[-15°, 15°]$ reduces the input range. By analyzing the output data, $|\theta_r - \theta_l| < 20°$ is a safe range that prevents the mechanical joints from breaking.

C. Payload Testing

To estimate the maximum payload of this prototype, assuming there are three forces that have the same magnitude $|\boldsymbol{f}|$ and corresponding lever arms: $\boldsymbol{r}_{f1} = [-50 \text{ mm}, 100 \text{ mm}, 0]^T$, $\boldsymbol{r}_{f2} = [0, 200 \text{ mm}, 0]^T$, and $\boldsymbol{r}_{f3} = [70 \text{ mm}, 320 \text{ mm}, 0]^T$.

Following the steps introduced in Section III, $\{\theta_r, \theta_l\}$ are inputs with resolution of $10°$, limited by $|\theta_r - \theta_l| < 20°$. The maximum torques acting on the two motors at all possible

(a)

(b)

Fig. 8. Scenario of payload testing.

positions are computed: $\tau^R_{max} = \max\mathcal{T}_R(140°, 120°) \simeq 0.258 \cdot |\boldsymbol{f}|$ and $\tau^L_{max} = \max\mathcal{T}_L(120°, 140°) \simeq 0.316 \cdot |\boldsymbol{f}|$.

Remark 4. The result shows the peak value of motor torque acting on the left motor q_{l1}, which is reasonable because the payloads contribute more gravity at the left side.

The SSPS-105 motor has 37 N·m maximum output torque under 100 W power input. Thus, $\|\boldsymbol{f}\|_\infty = 37/0.316 \simeq 117$ N. In case there are three forces, the maximum payload is 3×117 N$= 351$ N, meaning that the designed platform can afford goods with a weight of around 35.8 kg.

Fig. 8 shows the scenario of payload testing, where the designed platform is installed on the AGV for stair climbing. In Fig. 8 (a), several heavy goods (around 25 kg) are stacked up on the AGV. (Limited by the size of the platform and the maximum payload of the used AGV, 25 kg is the largest load that has been tested, even though 35.8 kg is the theoretical maximum payload for the platform.) In Fig. 8 (b)), the AGV is climbing the stairs with goods on the platform, where the platform adjusts its orientation according to the feedback information from IMU, validating the effectiveness of the designed platform.

V. Conclusion

This paper proposed a novel PKM, a two DOF self-balancing platform, for AGV to perform stable stair climbing in goods delivery processes. A detailed design method is provided, including the overall design and the structure determination method based on the design of pitch and roll angles of the platform. In addition, based on the designed structure, the static force analysis is also discussed. Finally, a simulation of the forward kinematics and the maximum payload (35.8 kg) of the mechanism are also conducted and concluded, where a demonstration of the prototype installed on an AGV is also presented to validate the performance of goods delivery when the AGV is moving on the stairs.

In the future, several aspects of the developed self-balancing platform can be improved. More cost-effective mechanical components with torsional or compression spring will be integrated to increase its maximum payloads instead of using high-payload motor. Besides, the theoretical methods proposed will also be used in designing a higher duty self-balancing platform for construction robots. Finally, a more comprehensive on-site testing will be conducted to validate the performance of the platform.

References

[1] C. Weng, Q. Yuan, F. Suárez-Ruiz, and I. Chen, "A telemanipulation-based human–robot collaboration method to teach aerospace masking skills," *IEEE Transactions on Industrial Informatics*, vol. 16, no. 5, pp. 3076–3084, 2020.

[2] C.-Y. Weng, W. Yin, Z. J. Lim, and I.-M. Chen, "A framework for robotic bin packing with a dual-arm configuration," in *IFToMM World Congress on Mechanism and Machine Science*. Springer, 2019, pp. 2799–2808.

[3] R. K. Katzschmann, J. DelPreto, R. MacCurdy, and D. Rus, "Exploration of underwater life with an acoustically controlled soft robotic fish," *Science Robotics*, vol. 3, no. 16, p. eaar3449, 2018.

[4] C.-Y. Weng, W. C. Tan, and I.-M. Chen, "A survey of dual-arm robotic issues on assembly tasks," in *ROMANSY 22–Robot Design, Dynamics and Control*. Springer, 2019, pp. 474–480.

[5] H. Wang, Y. Pan, S. Li, and H. Yu, "Robust sliding mode control for robots driven by compliant actuators," *IEEE Transactions on Control Systems Technology*, vol. 27, no. 3, pp. 1259–1266, 2019.

[6] R.-J. Yan, E. Kayacan, I.-M. Chen, L. K. Tiong, and J. Wu, "Quicabot: Quality inspection and assessment robot," *IEEE Transactions on Automation Science and Engineering*, vol. 16, no. 2, pp. 506–517, 2018.

[7] C. Theeravithayangkura, T. Takubo, Y. Mae, and T. Arai, "Stair recognition with laser range scanning by limb mechanism robot "asterisk "," in *2008 IEEE International Conference on Robotics and Biomimetics*. IEEE, 2009, pp. 915–920.

[8] J. Yuan and S. Hirose, "Research on leg-wheel hybrid stair-climbing robot, zero carrier," in *2004 IEEE International Conference on Robotics and Biomimetics*. IEEE, 2004, pp. 654–659.

[9] R. C. Luo, M. Hsiao, and T.-W. Lin, "Erect wheel-legged stair climbing robot for indoor service applications," in *2013 IEEE/RSJ International Conference on Intelligent Robots and Systems*. IEEE, 2013, pp. 2731–2736.

[10] M. Lehner, "Stair-climbing wheelchair carrier with crawlers," Feb. 6 1990, uS Patent 4,898,256.

[11] W.-S. Lee, J.-H. Kim, and J.-H. Cho, "A driving simulator as a virtual reality tool," in *Proceedings. 1998 IEEE International Conference on Robotics and Automation (Cat. No. 98CH36146)*, vol. 1. IEEE, 1998, pp. 71–76.

[12] C. Zhang and L. Zhang, "Kinematics analysis and workspace investigation of a novel 2-dof parallel manipulator applied in vehicle driving simulator," *Robotics and Computer-Integrated Manufacturing*, vol. 29, no. 4, pp. 113–120, 2013.

[13] N. Liu and J. Wu, "Kinematics and application of a hybrid industrial robot-delta-rst," *Sensors & Transducers*, vol. 169, no. 4, p. 186, 2014.

[14] I.-M. Chen, H.-H. Pham, and H.-C. Yeh, "Micro-motion selective-actuation xyz flexure parallel mechanism: design and modeling," *Journal of Micromechatronics*, vol. 3, no. 1, pp. 51–73, 2005.